The Astrophysical Journal, 683:1192–1206, 2008 August 20

TOPOLOGICAL EVOLUTION OF A FAST MAGNETIC BREAKOUT CME IN THREE DIMENSIONS

B. J. Lynch,[1] S. K. Antiochos,[2] C. R. DeVore,[3] J. G. Luhmann,[1] and T. H. Zurbuchen[4]

Received 2008 April 1; accepted 2008 April 28

ABSTRACT

We present the extension of the magnetic breakout model for CME initiation to a fully three-dimensional, spherical geometry. Given the increased complexity of the dynamic magnetic field interactions in three dimensions, we first present a summary of the well known axisymmetric breakout scenario in terms of the topological evolution associated with the various phases of the eruptive process. In this context, we discuss the analogous topological evolution during the magnetic breakout CME initiation process in the simplest three-dimensional multipolar system. We show that an extended bipolar active region embedded in an oppositely directed background dipole field has all the necessary topological features required for magnetic breakout, i.e., a fan separatrix surface between the two distinct flux systems, a pair of spine field lines, and a true three-dimensional coronal null point at their intersection. We then present the results of a numerical MHD simulation of this three-dimensional system where boundary shearing flows introduce free magnetic energy, eventually leading to a fast magnetic breakout CME. The eruptive flare reconnection facilitates the rapid conversion of this stored free magnetic energy into kinetic energy and the associated acceleration causes the erupting field and plasma structure to reach an asymptotic eruption velocity of $\gtrsim$1100 km s^{-1} over an $\sim$15 minute time period. The simulation results are discussed using the topological insight developed to interpret the various phases of the eruption and the complex, dynamic, and interacting magnetic field structures.

Subject headings: MHD — Sun: corona — Sun: coronal mass ejections (CMEs) — Sun: magnetic fields

1. INTRODUCTION

The magnetic breakout model (Antiochos et al. 1999) continues to be one of the leading theories for explaining the initiation of coronal mass ejections (CMEs). While formulated and first demonstrated in an axisymmetric (2.5 dimensional [2.5D]) spherical geometry, the same physical mechanisms invoked by the axisymmetric breakout scenario could, and should, take place in a fully three-dimensional (3D) system with a sufficient level of magnetic complexity. The most generic, nontrivial three-dimensional magnetic configuration is the field of two dipole (or dipole-like) sources. The resulting field configuration gives a two-flux system with two distinct polarity inversion lines (PILs), a domelike separatrix surface at the interface of the two flux systems, and a single null point at the intersection of the spine field lines with the separatrix surface (see Fig. 1 in Antiochos 1998). Given that this 3D magnetic configuration is fundamentally simpler than the quadrupolar axisymmetric system, the magnetic breakout process in 3D now involves the transfer of flux within each system from one "side" of their respective PILs to the other. In this sense, a 3D two-flux system can act in an analogous fashion to the axisymmetric four-flux system in that the transfer of restraining flux from above the expanding, low-lying sheared field in both the local and background flux systems is a runaway process leading to the eruption/opening of some portion of the field associated with the stressed flux system.

There is a growing body of theoretical and numerical work confirming the viability and robustness of the magnetic breakout model model. Previous numerical simulations of axisymmetric quadrupolar field configurations have shown catastrophic eruptions of stressed, low-lying field (Antiochos et al. 1999; MacNeice et al. 2004; Lynch et al. 2004) and a quantitative description of the free magnetic energy parameterized by the amount of reconnection available to the system has been developed (DeVore & Antiochos 2005). Phillips et al. (2005) showed that for axisymmetric multipolar configurations, a net-zero magnetic helicity shearing pattern could still produce a catastrophic eruption and that the magnetic free energy was the driving factor in the breakout scenario. Zhang et al. (2006) examined the role of both the breakout and eruptive flare reconnection in quadrupolar systems obtaining different velocity profiles depending on which current sheet was allowed to reconnect first. The breakout model has been shown to facilitate eruptions from energized side arcades of axisymmetric multipolar configurations (Gao et al. 2004), and recent work has gone into the role of breakout reconnection and flux-transfer to initiate "sympathetic" CMEs from topologically connected or adjacent energized flux systems (DeVore & Antiochos 2006; Peng & Hu 2007). Van der Holst et al. (2007) has presented a numerical simulation of an axisymmetric breakout eruption with a full solar wind model and shown the eruption disrupts (and detaches) the overlying helmet streamer. Recent simulations by DeVore & Antiochos (2008) have shown the breakout process works in a true 3D system with four distinct flux systems and a null line that intersects the boundary, yielding homologous eruptions when the system is continually energized. Roussev et al. (2007) have also exploited complex topology to generate breakout-like behavior for simulations of the 2002 April 21 and August 24 CME events, starting their simulations with actual magnetogram field observations. Since observed magnetic field configurations are often remarkably complex, making it difficult to get a handle on the underlying physics of the eruption in these cases, our approach in the current work is to concentrate on the simplest 3D field that can facilitate the breakout initiation model, in order to increase our understanding of the eruption process itself.

There are many observational studies that appear to agree with the breakout initiation scenario (e.g., Aulanier et al. 2000; Wang et al. 2002; Sterling & Moore 2001, 2004; Manoharan & Kundu,

[1] Space Sciences Laboratory, University of California-Berkeley, Berkeley, CA 94720.
[2] NASA Goddard Space Flight Center, MC 674, Greenbelt, MD 20771.
[3] Laboratory for Computational Physics and Fluid Dynamics, Naval Research Laboratory, Washington, DC 20375.
[4] Atmospheric, Oceanic, and Space Sciences Department, University of Michigan, Ann Arbor, MI 48109.

2003; Gary & Moore 2004; Deng et al. 2005; Pohjolainen et al. 2005; Liu et al. 2006; Joshi et al. 2007). Meanwhile, others find a mixture of breakout-compatible and -incompatible eruptions (e.g., Li and Luhmann 2006; Ugarte-Urra et al. 2007), and there are some events that, while compatible with magnetic breakout, are either not definitive (Li et al. 2008; Yurchyshyn et al. 2006) or the observers choose to draw different conclusions (Bong et al. 2006). Schrijver et al. (2008) claim there are some observations of the rapid acceleration phase associated with the transition from rising- to erupting-filament/prominence material in the low corona that previous magnetic breakout results were not able to reproduce. In addition, there continues to be misunderstanding about the capability of the breakout model to produce fast CMEs, despite the MacNeice et al. (2004) results showing the eruption process occurs at the characteristic Alfvén speeds of the simulation. This is partly due to, as mentioned by Forbes (2006) in a recent review, the fact that we have yet to quantitatively compare the breakout model to any real event. The results presented herein represent significant progress toward this aim because in this simulation, while still an idealized calculation, we now have sufficiently large Alfvén speeds in the sheared field region that our eruption velocities could be directly compared to the $\sim$1000 km s^{-1} velocities of fast CMEs derived from coronagraph observations.

The structure of the paper is as follows. In § 2 we will first review the standard (2.5D) breakout eruption process in the context of the topological evolution of the system and then go through breakout in a fully three dimensional geometry, highlighting the analogous topological changes associated with each phase of the eruptive process. In § 3 we present results of a numerical MHD simulation of breakout CME initiation which produces a highly complex erupting field structure, the dense leading edge and depleted cavity region often seen in coronagraph observations of three-part CMEs, and a two stage height-time profile that shows a remarkably sharp transition to a uniform eruption velocity of $\gtrsim$1100 km s^{-1}. We continue by briefly discussing the current sheet formation and 3D magnetic reconnection associated with both the magnetic breakout and eruptive flare reconnection and the evolution of the magnetic and kinetic energy of the system. In § 4 we close with a discussion of future work.

2. TOPOLOGICAL EVOLUTION OF THE BREAKOUT INITIATION SCENARIO

2.1. *2.5 Dimensions*

Figure 1 shows both a schematic of the four main stages of the breakout model mechanism for CME initiation (*left*) and the corresponding snapshots of the MHD numerical simulation results of MacNeice et al. (2004). Figure 1*a* shows the initial potential field state of the axisymmetric multipolar topology and the associated topological features of the four-flux system. The field lines are colored in the manner of Antiochos et al. (1999), and the surface extent of each flux system is shaded on the disk in light blue, green, and red. The separatrix surfaces between the different flux systems are drawn in black and the intersection of these surfaces with the $r = R_\odot$ inner boundary are indicated as solid black lines on the disk face. The coronal null point (really a null line in 2.5D) is defined as the intersection of these surfaces in the corona. The three PILs are also drawn as dashed lines on the disk face. The dark blue region surrounding the equatorial PIL indicates the narrow shearing channel where the energization of the system will occur by imposing ideal azimuthal shearing flows.

Figure 1*b* shows the energization and magnetic breakout phase of the eruptive process. The inner flux system expands due to the increase in magnetic pressure associated with introducing a non-zero ϕ-component and the X-type null point (line) becomes distorted. Volumetric currents start to build up along the separatrix surfaces and are concentrated between the oppositely directed blue and red flux systems. In the numerical MHD simulations, once the current sheet structures are compressed to the scale of the computational grid, numerical diffusion acts as a localized increase in magnetic resistivity and allows magnetic reconnection, to "switch on." Reconnection enables the transfer of magnetic flux from the inner and overlying systems (*blue and red regions*) to the (*green region*) side-lobe arcades. The loss of restraining field above the shear channel allows increasingly rapid expansion which in turn drives increasingly faster magnetic reconnection. The positive feedback loop between expansion and magnetic breakout reconnection, also called "external" reconnection (Moore et al. 2001), leads to the catastrophic expulsion of the low-lying sheared field to infinity and is the defining physical process of the breakout mechanism for CME initiation.

The consequences of the flux transfer and accumulation in the green side-lobe arcades is that the separatrix surfaces evolve in time, and therefore, the boundaries between flux systems on solar surface move in response to the coronal activity. In other words, the breakout reconnection phase can be characterized by the inner side-lobe separatrix boundaries moving toward the shear channel (as unsheared light blue flux is transferred) and the outer side-lobe separatrix boundaries move toward the poles (as overlying red flux is transferred). This topological evolution is shown as pairs of green arrows to the left of the disk surface.

Figure 1*c* shows the eruptive flare reconnection that starts deep in the shear channel. In the breakout model, this "internal" reconnection (Moore et al. 2001) is a direct consequence of the runaway expansion via the formation and lateral compression of a radial current sheet between the oppositely directed legs of expanding sheared field, and is driven by the magnetic breakout reconnection. This phase of the breakout mechanism is the standard CHSKP flare reconnection (Carmichael 1964; Hirayama 1974; Sturrock 1968; Kopp & Pneuman 1976), which is common to all models of CME initiation (e.g., Linker et al. 2003; Forbes & Lin 2000; Roussev et al. 2004, 2007). The flare reconnection has two main effects. First, in the breakout model, the entire erupting structure is processed through the flare reconnection region, and this has the consequence of imparting a high degree of twist to the erupting fields, transforming the expanding sheared arcade into a flux rope configuration during the eruption. A limitation of the axisymmetric simulations is that the flare reconnection creates truly disconnected field lines, we will show that in 3D the erupting structure resembles a flux rope with both footpoints anchored at the solar surface. Second, the flare reconnection rebuilds the central blue arcade underneath the erupting sheared field and attempts to return the system to a more potential state. It should also be noted that this creates another separatrix surface and a new null point underneath the opening field of the inner arcade. The blue arrows indicate the motion of the newly formed separatrix that defines the boundary of the unsheared (or significantly less sheared) "flare loops" (*light blue region*) with the erupting field (*dark blue region*) in the process of opening to infinity. The flare reconnection allows for the most efficient conversion of stored magnetic free energy into kinetic, thermal, and gravitational energy.

Figure 1*d* shows the final relaxation stage of the multiflux systems in the wake of the eruption as well as the propagation stage of the ejecta itself. The eruptive flare reconnection depicted in Figure 1*c*, when acting on the fields in the shear channel is fast and energetic, corresponding to the often observed "impulsive" phase of flares. Once the entire shear channel field has been

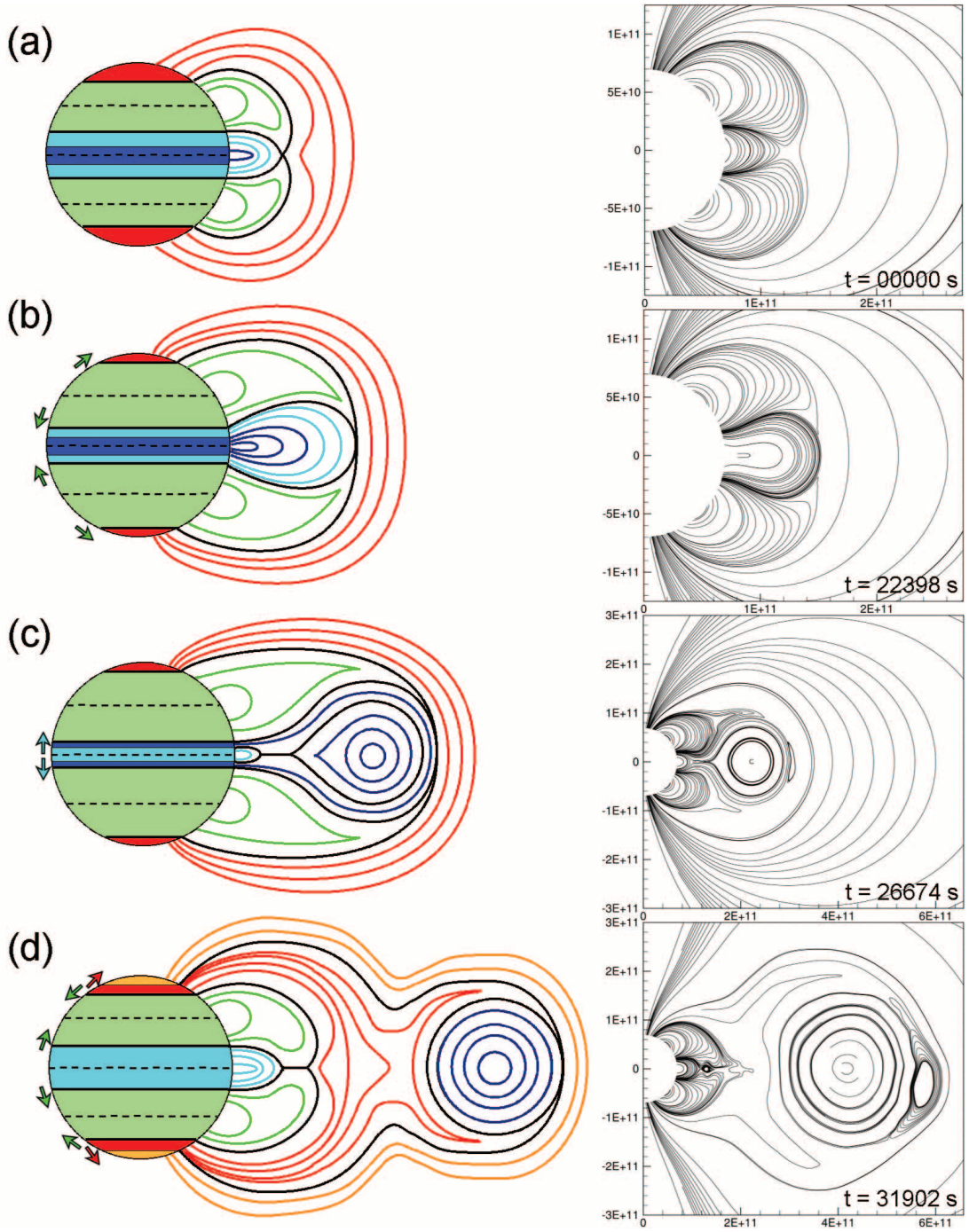

FIG. 1.—*Left*: Schematic showing the main four stages of topological evolution during the axisymmetric (2.5D) breakout CME scenario. (*a*) Initial topology and the shear channel, (*b*) Shearing phase required to energize the system and the onset of magnetic breakout reconnection at the distorted null line, (*c*) Beginning of flare reconnection that starts deep in the shear channel and creates the magnetic flux rope, and (*d*) Antibreakout reconnection phase that describes the system relaxation and topological restoration. *Right*: Corresponding field line plots from the MacNeice et al. (2004) MHD simulation. See text for further details.

processed, the side arcades come together and reconnect at the flare current sheet. These side-lobe fields tend to be much less sheared and their reconnection proceeds in a slower, less energetic manner corresponding to the "gradual" phase often observed in flares. When the (*green region*) side-lobe fields reconnect, they restore both the inner (*light blue region*) and overlying (*red region*) flux systems—denoted by the green arrows showing the side-lobe separatrix surfaces shrinking. Since this topological evolution is the reverse of the original breakout reconnection, one can think of the posteruption restoration of the original flux system configuration as "antibreakout" reconnection. The antibreakout reconnection eventually dissipates the radial current sheet and eventually restores the coronal null point.

The erupting flux rope structure continues to propagate through the background dipole field lines, and in our axisymmetric picture, this means continual breakout reconnection at the interface of the oppositely oriented flux rope configuration and the overlying field. However, there is an important topological distinction to be made between the overlying field that has yet to encounter the ejecta and that which has either been reformed behind the flux rope (from antibreakout reconnection) or has recently encountered the flux rope and has undergone reconnection such that it now

closes behind the ejecta. This distinction is denoted in the figure by coloring the background field lines that have yet to encounter the flux rope and their surface flux distribution orange. A dynamic separatrix-like surface exists between the ejecta flux system, the original overlying (*red region*) system, and the (*orange region*) background fields. The orange flux system corresponds to overlying field "opened" by the eruption, and should be observable as remote dimming regions or the evolution of the coronal hole boundaries (e.g., Attril et al. 2006, 2007). Both the continued propagation of the CME (and its interaction with the background field) and the antibreakout reconnection above original source arcade play a role in restoring the original overlying (*red region*) flux system.

2.2. *Three Dimensions*

Figure 2 is the schematic of the analogous stages of the topological evolution of magnetic breakout in a fully three dimensional system. Each panel corresponds to the phase of the eruptive process described in § 2.1 for the axisymmetric case.

Figure 2*a* plots the initial magnetic features corresponding to two distinct flux systems. The polarity inversion lines are again shown as dashed lines on the disk. In three dimensions, the boundary between flux systems is a domelike separatrix surface that encompasses the entire flux closing over the local active region PIL. The intersection of this separatrix surface is again shown as the solid line on the disk face. There are two spine field lines, one originating in the opposite polarity spot of the active region flux system and "closes" as the separatrix surface, the other originating in the southern hemisphere, also "closing" as the separatrix surface. The coronal null point is initially where the spine lines meet. The intersection of the spine lines with the solar surface is indicated by the solid black dots. The evolution of the spine field line in three dimensions will correspond to the evolution of one of the separatrix surfaces in the axisymmetric configuration, but as a line instead of a planar structure.

In this simple geometry, the active region flux system consists of field that plays the role of both the inner-arcade (*blue line*) and the upper side-arcade (*green line*) flux systems with the overlying background field playing the roles of the lower side arcade (*green line*) and overlying flux system (*red line*) in the axisymmetric scenario. The highly concentrated shear channel (*dark blue stripe*) now only extends over a portion of the active region polarity inversion line.

Figure 2*b* shows the surface evolution of the AR separatrix dome and spine field line during the breakout reconnection process. Magnetic reconnection at a current sheet formed at the distorted null point reconnects blue and red flux, shifting overlying unsheared field from one side of the AR flux system to the other and likewise, from one side (*red region*) of the background flux system to the other (*green region*). The additional flux deposited over the respective portions of the PILs shift the separatrix dome boundary one way and the spine field lines the opposite direction. The net result being completely analogous to the 2.5D evolution. The system is minimizing the amount of unsheared field it will be required to open when it ejects the low-lying sheared flux. The positive feedback between expansion of the stressed inner-arcade half of the AR flux system and the rate of breakout reconnection at the null point eventually leads to the explosive eruption and flare reconnection stage.

Figure 2*c* depicts the eruptive flare reconnection expected in 3D breakout. The orange regions on the disk face represent the footpoints of the erupting structure because without the axisymmetry that creates truly disconnected flux, every field line is still rooted at the solar surface. The two footpoints on opposite sides

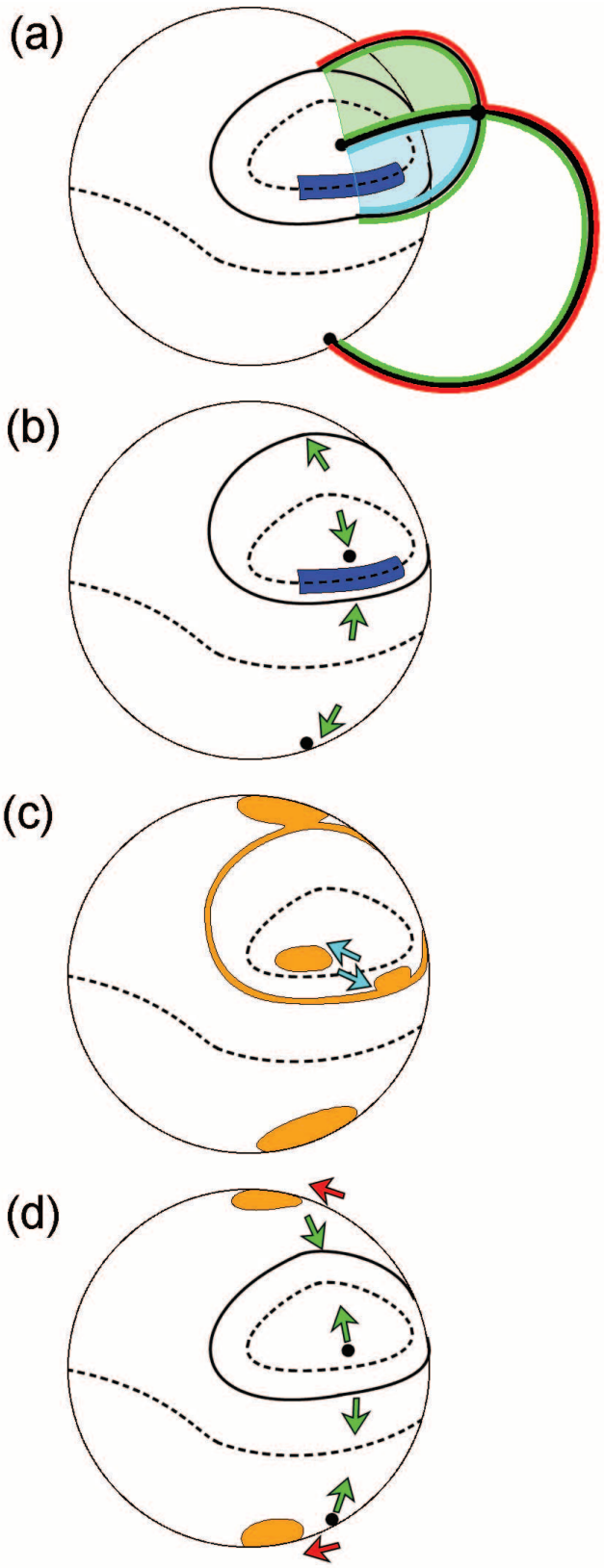

FIG. 2.— Schematic of the topological evolution during the 3D breakout CME scenario corresponding to the same four stages described in Fig. 1. See text for further details.

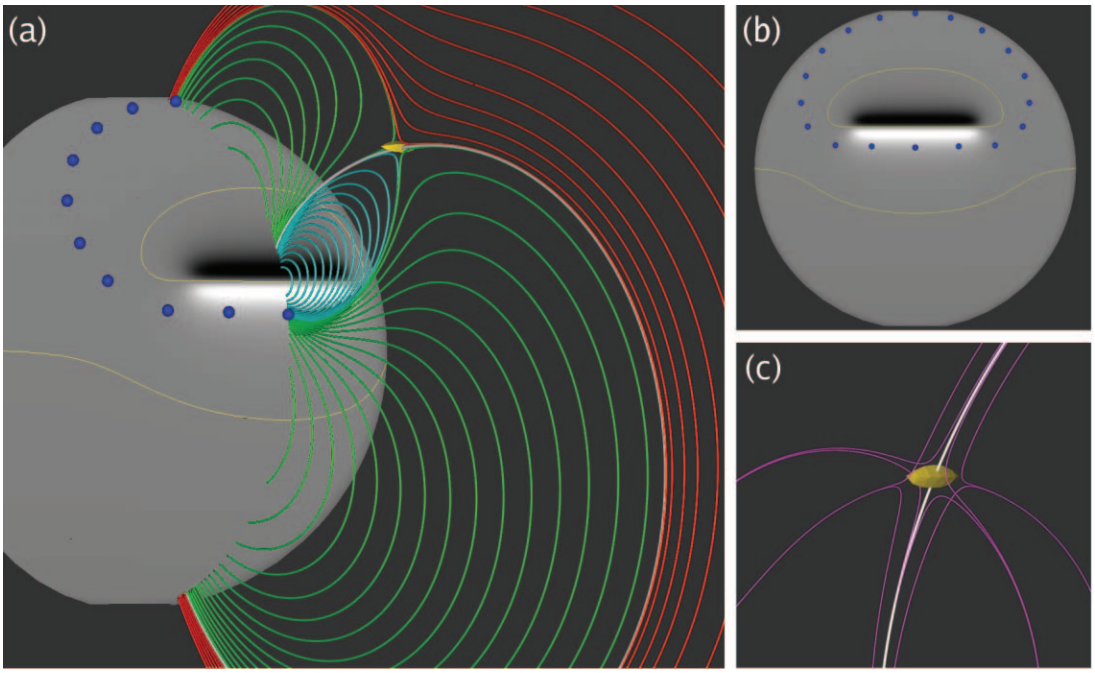

FIG. 3.—(*a*) Initial 3D magnetic field configuration for the MHD simulation described in § 3.2.1. Magnetic field lines are drawn in the symmetry plane and colored in the Antiochos et al. (1999) fashion. The thin yellow lines on the solar surface are the two distinct magnetic polarity inversion lines. (*b*) Azimuthal extent of the elongated active region and the separatrix boundary on the solar surface. (*c*) Zoomed-in view of the field line connectivity in the vicinity of the spine field line (*white area*) and the 3D coronal null point (depicted as the yellow isosurface of the plasma $\beta = 2000$).

of the active region PIL are obvious, but in three dimensions in order to open field inside a separatrix, the entire separatrix surface must open as well. This means that both the spine field line and the entire separatrix dome must open temporarily as the system ejects the stressed, sheared field. Every boundary between open (*orange region*) and closed (*white region*) field is a separatrix surface. In the process of opening, the spine lines have become a finite area region. This configuration corresponds exactly to the nesting conjecture discussed in detail by Antiochos et al. (2007) in the context of the steady state magnetic configuration of low-latitude coronal holes. Despite our dynamic and energetic evolution, opening the entire separatrix dome surface, even temporarily, must lead to the opening a narrow channel (possibly measure zero) of field extending to the footpoints of flux in the background system also being opened during the eruption process. This narrow, open field is identical to the postulated channels of open field connecting seemingly disconnected coronal holes in the same polarity region (Antiochos et al. 2007).

The internal flare reconnection acts to erode the footpoints of the erupting structure while attempting to rebuild the portion of the AR flux system catastrophically disturbed by the eruption of sheared field. The newly formed field lines below the erupting structure are much more potential and the blue arrows indicate the flare loop arcade growth along the PIL. The flare reconnection can also impart a tremendous amount of twist onto the erupting, initially untwisted sheared field. Completely analogous to the axisymmetric case, a twisted, and possibly highly twisted flux rope like structure is created during the eruption process and a consequence of the flare reconnection.

Figure 2*d* corresponds to the final relaxation phase in three dimensions. The vast majority of the inner arcade (*light blue region*) has been restored by the eruptive flare reconnection and we enter the antibreakout phase of the system's flux rearrangement. The upper (*green region*) half of the active region flux system continues to unload its excess flux onto the lower half (*light blue*), and the global background flux system does likewise (from the lower green flux to overlying red flux). The connectivity of the erupting sheared flux has been completely eaten away through interchange reconnection (e.g., Gosling et al. 1995; Crooker et al. 2002; Owens et al. 2006) from either side of the original AR PIL and now connects to the polar open field regions representing either coronal holes (in the presence of global open field) or in our case the amount of background flux carried out along with the eruption. The spine line is the last "open" field line that closes back down in the wake of the ejection of the low-lying sheared field, signaling the simultaneous restoration of the separatrix dome enclosing the entire active region flux. The location of the spine line footpoints will continue to evolve with continued antibreakout reconnection. The remote open-field regions are also eaten away as the ejecta propagates out to infinity through the continued interaction of the breakout reconnection on the front side of the erupting flux and antibreakout reconnection beneath the erupting structure. Note that this discussion implies that there is likely to be two timescales for the decay of flux added to the heliosphere by a CME, a fast timescale corresponding to flare reconnection and a potentially much longer timescale corresponding to the slow antibreakout reconnection of the distant open regions.

Figure 3 plots the initial 3D magnetic field configuration of the MHD simulation and all of the various topological features described in the first panel of Figure 2. Here, Figure 3*a* plots the radial field at the inner boundary in gray scale along with a series of representative field lines in the meridional plane of symmetry. The yellow lines on the solar surface indicate the two magnetic PILs belonging to the extended AR and global background flux systems. The blue dots indicate the spatial location of the intersection of the separatrix dome surrounding the AR flux system with the solar surface. The spine field line is colored white and the yellow isosurface of plasma $\beta = 2000$ indicates the 3D coronal null point. Figure 3*b* shows the azimuthal extent of the strong-field active region and the separatrix boundary. Figure 3*c* shows a zoomed-in view of the coronal null point. While the numerical simulation is truly three dimensional, we have chosen this latitudinally extended

dipolar configuration which is, in a sense, quasi-two-dimensional, for two reasons. First, to reproduce as much as possible the behavior seen in the axisymmetric case and therefore, significantly ease our interpretation of the results and assist in drawing the analogy between the two. Second and more importantly, all erupting filament channels are long with respect to the width of the highly concentrated shear zone surrounding the PIL. The reason is that for a large free energy to build up in a 3D geometry, the length of low-lying sheared field lines must be large compared to that of overlying unsheared field lines, otherwise the overlying field can simply move aside, allowing the sheared field to rise freely. This restriction on the relative lengths of the sheared and overlying field lines implies that a filament channel must be long compared to its width. Note that this result is a key difference between a 3D and a 2D geometry, because field lines (actually surfaces) can never move aside in 2D, so that in principle there is no restriction on the length to width ratio of erupting 2D filament channels. The details of the construction of our 3D field configuration are described further in § 3.2.1.

3. MHD SIMULATION OF 3D BREAKOUT

3.1. *Numerical Methods*

The Adaptively Refined MHD Solver (ARMS) code calculates solutions to the nonlinear, coupled, time-dependent partial differential equations of magnetohydrodynamics. The MHD equations describe the temporal evolution and transport of density, momentum, and energy throughout the plasma and include the induction equation for the evolution of the magnetic field. We also require an equation of state for the plasma that closes the system of equations. The equations of ideal MHD are thus,

$$\frac{\partial \rho}{\partial t} + \nabla \cdot \rho \boldsymbol{v} = 0, \tag{1}$$

$$\frac{\partial \rho \boldsymbol{v}}{\partial t} + \nabla \cdot \rho \boldsymbol{v} + \nabla p = \frac{1}{4\pi}(\nabla \times \boldsymbol{B}) \times \boldsymbol{B} - \rho \boldsymbol{g}, \tag{2}$$

$$\frac{\partial T}{\partial t} + \nabla \cdot T \boldsymbol{v} = (2 - \gamma) T \nabla \cdot \boldsymbol{v}, \tag{3}$$

$$\frac{\partial \boldsymbol{B}}{\partial t} = \nabla \times (\boldsymbol{v} \times \boldsymbol{B}), \tag{4}$$

where ρ is the mass density, $\boldsymbol{v}$ is the velocity, $\boldsymbol{B}$ is magnetic induction, T is the temperature, and the ratio of specific heats is $\gamma = 5/3$. For the plasma equation of state, we use the ideal gas law, $p = 2(\rho/m_p)k_{\rm B}T$ with $k_{\rm B}$ being Boltzmann's constant and m_p being the proton mass. The solar gravitational acceleration is $\boldsymbol{g} = g_\odot (R_\odot/r)^2 \hat{r}$.

There is no explicit magnetic resistivity in the above equations, but necessary and stabilizing numerical diffusion terms introduce an effective resistivity on very small spatial scales, i.e., the size of the grid. In this way, magnetic reconnection can occur when magnetic null points or current sheet features have been distorted or compressed to the local grid scale.

The numerical scheme used is a finite-volume, multidimensional flux-corrected transport (FCT) algorithm in spherical coordinates, developed by DeVore (1991). The spatial storage location of the fields, velocities, and fluxes in each cell are staggered such that the FCT formulation guarantees $\nabla \cdot \boldsymbol{B} = 0$ to machine accuracy. The code is formally second-order accurate in space and time for a uniformly spaced grid. The ARMS code is fully integrated with the adaptive mesh toolkit PARAMESH (MacNeice et al. 2000) to handle dynamic, solution-adaptive spherical grid refinement and support multiprocessor parallelization.

Figure 4 shows the numerical grid used for the calculation. The grid refinement levels have been calculated to best resolve the boundary flows and the active region shear channel. In this simulation the grid remains static after this initial refinement at $t = 0$ s. Figure 4*a* shows the full computational domain: $1\ R_\odot \le r \le 20\ R_\odot$, $0.0625\pi \le \theta \le 0.9375\pi$, and $-0.5\pi \le \phi \le 0.5\pi$. The coarsest grid resolution in (r, θ, ϕ) is $80 \times 64 \times 64$ and there are three additional levels of grid refinement that each double the resolution for a total of approximately 4.5 million cells. The radial griding is logarithmic, so the $r : \theta : \phi$ aspect ratio remains constant throughout the computational domain in each refinement level. Figure 4*b* shows the finest grid, necessary for resolving the imposed boundary velocity pattern and the evolution of the low lying sheared flux. Figure 4*c* shows the azimuthal extent of the various refinement regions on the solar disk face.

3.2. *Initial Conditions*

3.2.1. *Magnetic Field*

We construct the latitudinally extended magnetic field configuration shown in Figure 3 by creating a distribution of twenty-eight magnetic dipoles, placed beneath the $r = 1\ R_\odot$ surface. The total initial field is the superposition of these magnetic field sources, $\boldsymbol{B}(\boldsymbol{r}) = \sum \boldsymbol{B}_i^{\rm dip}(\boldsymbol{r})$, with $i = 0$ to 27 and the standard dipole field of

$$\boldsymbol{B}_i^{\rm dip}(\boldsymbol{r}) = M_i \left(\frac{R_i^{\rm dip}}{|\boldsymbol{r} - \boldsymbol{r}_{0,i}|} \right)^3 [3\boldsymbol{n}_i(\boldsymbol{n}_i \cdot \boldsymbol{m}_i) - \boldsymbol{m}_i], \tag{5}$$

where $\boldsymbol{n}_i$ is a unit vector in the direction of $\boldsymbol{r} - \boldsymbol{r}_{0,i}$, $\boldsymbol{m}_i$ is the unit vector in the direction of the ith dipole moment, $R_i^{\rm dip}$ is the characteristic length scale, and M_i is the magnitude in units of Gauss. The global background dipole is located at the origin $\boldsymbol{r}_{0,0} = [0, 0, 0]$, pointing in the $\boldsymbol{m}_0 = \hat{z}$ direction with $M_0 = 1.0$ G and a length scale of $R_0^{dip} = 1\ R_\odot$. The spatial location (r, θ, ϕ) of each of the dipoles making up the elongated active region ($i = 1$ through 27) is given by

$$\boldsymbol{r}_{0,i} = \left[0.928571\ R_\odot, 0.41667\pi, 0.1274\pi \left(\frac{i - 14}{13} \right) \right], \tag{6}$$

each having characteristic length scales of $R_i^{\rm dip} = 0.342857\ R_\odot$, magnitudes $M_i = 0.150$ G, and oriented in the $\boldsymbol{m}_i = \hat{\theta}$ direction. The maximum active region field strength is approximately ± 25 G at the photosphere and the total ϕ range of the active region is $\sim 60^\circ$. The shearing flows are defined over a $\sim 12^\circ$ range in θ centered on the AR PIL, giving our shear channel a length-to-width ratio of 5 : 1.

3.2.2. *Solar Atmosphere*

For simplicity, we take a spherically symmetric solar atmosphere. The temperature profile is chosen such that it has an r^{-1} radial dependence. To satisfy the hydrostatic equilibrium conditions, the remaining atmospheric parameters must also have power-law forms. Thus, our complete plasma profiles are given by

$$T(r) = T_\odot \left(\frac{r}{R_\odot} \right)^{-1}, \quad p(r) = p_\odot \left(\frac{r}{R_\odot} \right)^{-\mu},$$
$$n(r) = n_\odot \left(\frac{r}{R_\odot} \right)^{-\mu+1}. \tag{7}$$

We choose the gas pressure exponent $\mu = R_\odot/H_\odot = 6.0$, where the pressure scale height defined as $H_\odot = 2k_{\rm B}T_\odot/m_p g_\odot$. Solar gravity at the surface is $g_\odot = 2.75 \times 10^4$ cm s^{-2}.

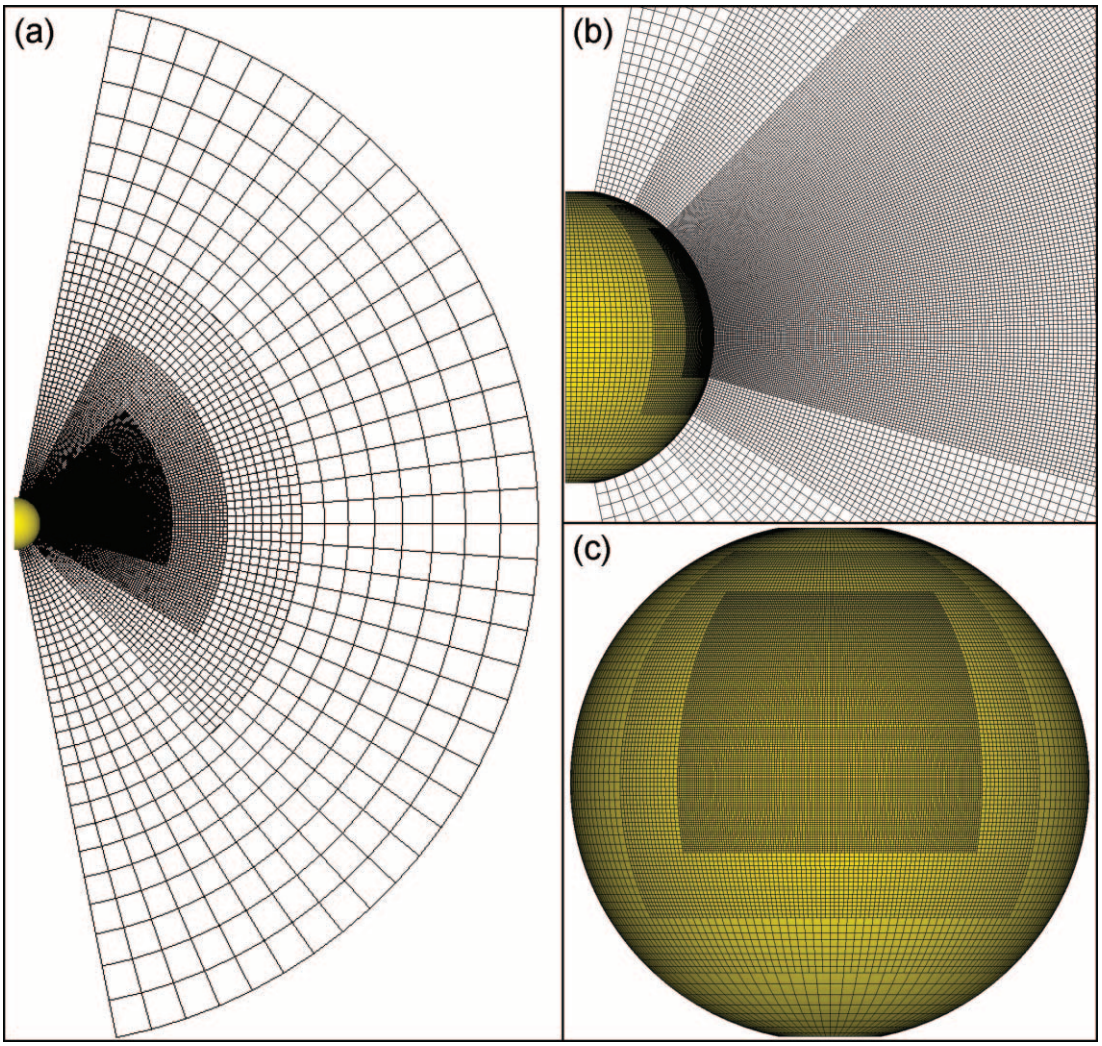

FIG. 4.—Static, nonuniform computational grid used in the MHD simulations. (*a*) Full domain, from the solar surface out to 20 $R_\odot$. (*b*) Highest grid resolution, centered on the active region and includes the coronal null point. (*c*) Azimuthal extent of the grid refinement regions on the disk face. The radial griding is logarithmic; consequently the $r : \theta : \phi$ aspect ratio in each cell is approximately constant throughout the entire domain.

The initial gas pressure at the surface is set at $p_\odot = 0.025$ dyn cm^{-2}, and the remaining initial surface quantities $T_\odot$ and $n_\odot$ are determined from the ideal gas law and the specified value of the pressure exponent, yielding $T_\odot = 1.943 \times 10^6$ K and $n_\odot = 4.659 \times 10^7$ cm^{-3}.

The solar atmosphere profiles of density, temperature, and gas pressure are chosen to keep the plasma $\beta = 8\pi p/B^2$ as reasonable as possible over the entire computational domain. At large distances, the magnetic energy is dominated by the background dipole field and falls off as r^{-6}, which motivated our choice for the pressure power-law exponent μ. In the strong field active region and along the shear channel during the simulation, $\beta \lesssim 0.001$, although it is of $O(3)$ at large distances (>5 $R_\odot$) and diverges approaching the null point.

Figure 5 plots both the radial dependence of the plasma β (*diamonds*) and Alfvén speed V_A (*triangles*) along a radial cut in the meridional plane of symmetry ($\phi = 0$) and at 14.75° latitude. This cut approaches the coronal null point located at $(r, \theta, \phi) = [1.8377\ R_\odot, 0.36328\pi, 0]$ and shows the significant spatial variation of both V_A and β, 3 and 4 orders of magnitude, respectively.

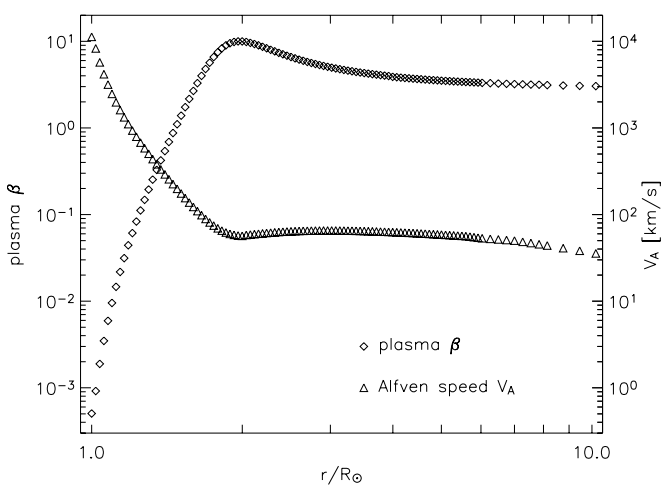

FIG. 5.—Plasma β (*diamonds*) and Alfvén speed V_A (*triangles*) along a radial cut at $\phi = 0$ and 14.75° latitude passing near (but not through) the coronal null point showing the strong radial dependence of these parameters in the strong-field filament channel transitioning to an approximately constant dependence far from the Sun.

3.2.3. *Boundary Shearing Flows*

The surface flow pattern on the inner radial boundary has been constructed to preserve the normal component of the magnetic field B_r at the surface. This ensures that the shearing motions only add

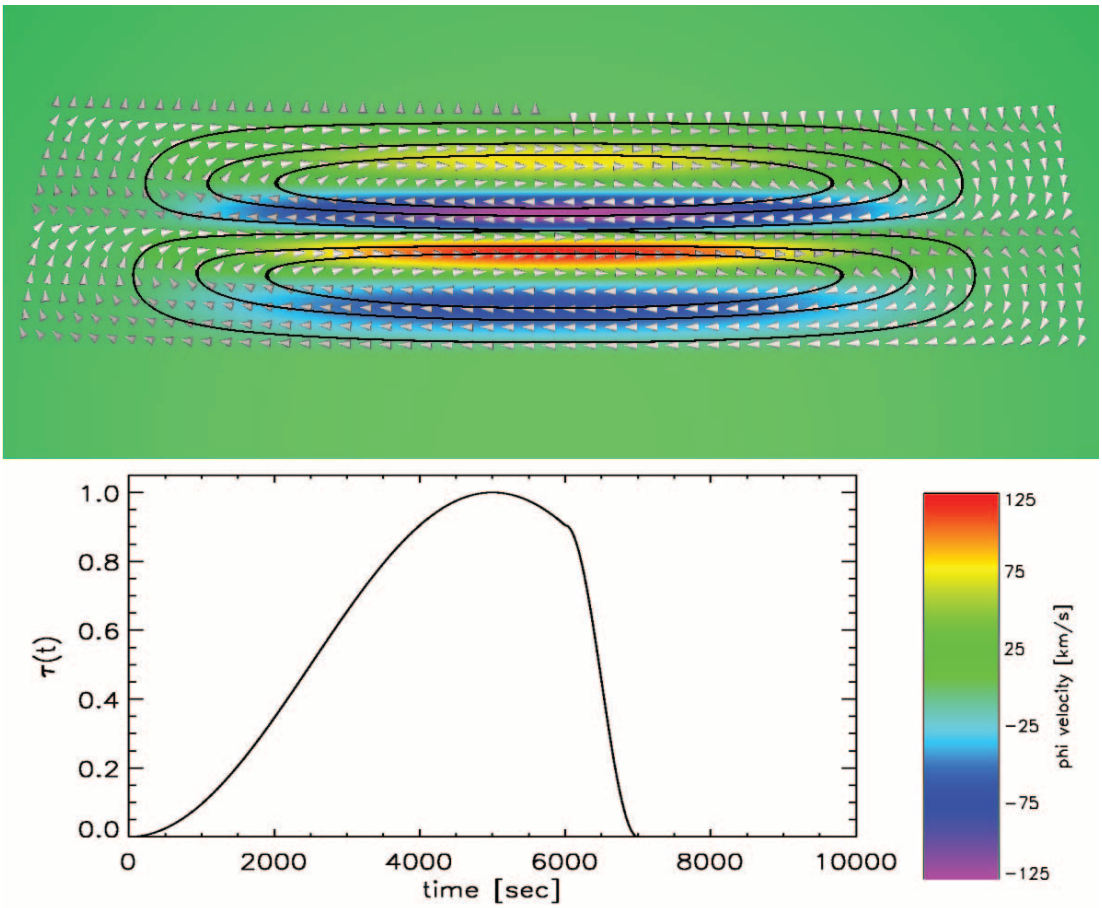

FIG. 6.— *Top*: Contour plot showing $v_\phi(\theta, \phi)$ on the inner boundary (color scale at lower right) of the highly localized shear channels. The arrows indicate the normalized vector direction and the black lines are velocity streamlines showing the circular pattern for each polarity of the filament channel. *Bottom*: Temporal dependence $\tau(t)$ of the applied flow field.

magnetic free energy to the system. However, due to the complicated spatial variation of B_r in the vicinity of the active region PIL, we must abandon the simple incompressible shearing flows used to drive the 2.5D simulations. The shearing motions in the 3D case can be calculated from the requirement

$$\frac{\partial B_r}{\partial t} + \nabla \cdot (B_r \boldsymbol{v}_\perp) = 0. \tag{8}$$

In order to have $\partial B_r/\partial t = 0$ satisfied, the velocity pattern must obey $\nabla \cdot (B_r \boldsymbol{v}_\perp) = 0$. Thus, it is convenient to have the $B_r \boldsymbol{v}_\perp$ be a curl of the radial unit vector multiplied by a scalar function,

$$\boldsymbol{v}_\perp(\theta, \phi, t) = \frac{1}{B_r} \nabla \times f(\theta, \phi, t)\hat{r}. \tag{9}$$

We choose the function $f(\theta, \phi, t) = V_0 B_r^3(\theta, \phi)\Theta(\theta)\Phi(\phi)\tau(t)$ so that $\boldsymbol{v}_\perp$ has a linear dependence on B_r (after the curl derivatives) and goes to zero at the PIL. The spatial and temporal extent of the driving flow is specified by the smooth functions $\Phi(\phi)$, $\Theta(\theta)$, and $\tau(t)$. The ϕ spatial dependence of the driving flow is a relatively straightforward sinusoid, given by

$$\begin{aligned}\Phi(\phi) &= (1 - \cos[2\pi(\phi + 0.17\pi)/0.34\pi]) \\ &\quad \times (1 - \cos[2\pi(\phi - 0.17\pi)/0.34\pi]), \\ &\quad \text{for } -0.17\pi \le \phi \le +0.17\pi, \\ \Phi(\phi) &= 0, \quad \text{otherwise.}\end{aligned} \tag{10}$$

The θ-filter also has a sinusoidal dependence, defined over the specified range $0.38\pi \le \theta \le 0.45333\pi$,

$$\begin{aligned}\Theta(\theta) &= 1 - \cos[2\pi(\theta - 0.38\pi)/0.03665\pi], \\ &\quad \text{for } 0.38\pi \le \theta < 0.41665\pi, \\ \Theta(\theta) &= 1 - \cos[2\pi(\theta - 0.41669\pi)/0.03665\pi], \\ &\quad \text{for } 0.41669\pi \le \theta \le 0.45333\pi, \\ \Theta(\theta) &= 0, \quad \text{otherwise.}\end{aligned} \tag{11}$$

The temporal dependence is a piecewise-continuous function, given by two sinusoids

$$\begin{aligned}\tau(t) &= 1 - \cos\left[2\pi t/10^4\right], \\ &\quad \text{for } 0 \le t < 6000, \\ \tau(t) &= 0.904582(1 - \cos[2\pi(t - 5000)/2000]), \\ &\quad 6000 \le t \le 7000 \\ \tau(t) &= 0, \quad \text{otherwise,}\end{aligned} \tag{12}$$

such that the shearing velocity reaches its maximum value at $t = 5000$ s and quickly ramps down to zero between $6000 < t < 7000$ s.

The top panel of Figure 6 shows the spatial dependence of the ϕ-component of the total shearing profile $\boldsymbol{v}_\perp(\theta, \phi, t)$ on the surface $r = 1\ R_\odot$. The arrows show the (normalized) direction of the vector flow field, and the black lines indicate flow streamlines depicting the oppositely directed shearing near the AR PIL and the structure of the return flows. The complexity of this shearing

pattern has a distinct imprint on the structure and complexity of the erupting sheared field. The bottom panel shows the multiplicative temporal dependence imposed on the surface flows. To minimize the computational time, V_0 is chosen such that the maximum shearing velocities reach approximately ± 130 km s^{-1} at $t = 5000$ s, but the average value over the 7000 s shearing phase is 65 km s^{-1}. Realistic photospheric velocities are of the order of $\sim$1 km s^{-1}, but the simulation driving motions are much, much less the than Alfvén speed in the strong field region at the solar surface ($\max[v_\perp]/\max[V_A] \lesssim 1.5\%$), so the system still evolves quasi-statically. The maximum boundary flow velocities do approach the sound speed near the surface ($\sim$164 km s^{-1}), so we expect a weak acoustic shock to form and propagate through the atmosphere in response to the driving. However, the runaway expansion and eruption dynamics are due to the rapid magnetic reconfiguration of the corona rather than a "directly driven" consequence of the boundary shearing flows. As we will see below, the resulting eruption velocities are more than an order of magnitude above the imposed surface flows.

3.3. *Results*

3.3.1. *Eruption Overview*

Figure 7 shows the evolution of the magnetic field in a series of field line plots. The field lines are all traced from the $\phi = 0$ plane and correspond to simulation times printed in the upper left-hand corner of each frame. The field lines are colored to match the 2.5D Antiochos et al. (1999) results for clarification of the role each "portion" of the two flux system plays. From this side view, the evolution looks quite similar to the axisymmetric case in that the expanding field reconnects all of the unsheared flux (*light blue field lines*) with the overlying flux (*red lines*) and transfers it to the portion of each flux system acting as the "side arcades" (*green lines*). The first two panels, $t = 4500$ and 6250 s, correspond to Figure 2*b*, the breakout reconnection stage before the eruptive flare reconnection. The next four panels, $t = 6750$, 7500, 8500, and 10,000 s, are all part of Figure 2*c*, showing the eruptive-flare opening of the highly sheared low-lying field. The simulation as of $t = 10{,}000$ s has not reached the antibreakout reconnection stage shown in Figure 2*d*, where the portions of the two flux systems acting as "side arcades" come back together to participate in the gradual phase of the eruptive flare reconnection and the rebuilding of the multipolar topology present before the energization of the system. The eruptive flare reconnection certainly adds a great deal of azimuthal (significantly twisted) flux to the erupting sheared field, creating a quasi–flux-rope-like ejecta. However, the complexity of our specified shearing flows creates a highly complex erupting structure in which the erupting ejecta field undergoes internal relaxation reconnection as it propagates away from the Sun, merging the oppositely sheared components.

Despite the complex and dynamic field interactions, both within the ejecta itself and between the ejecta and the overlying background field system, the density and velocity associated with our erupting structure takes on a much more classical appearance. Figure 8 shows meridional cuts of the plasma number density in the $\phi = 0$ plane for each of the times and perspectives in Figure 7. The simulation results produce a clear enhanced density font, defining the leading edge or separatrix boundary between the erupting flux and the background flux system.

By $t = 10{,}000$ s, the cavity region is about a factor 30 less dense than the initial $t = 0$ value at the same radial distance. Likewise, the enhanced density rim is about 30 times denser than the initial background value. Recent forward modeling of CME density structures to produce synthetic line-of-sight coronagraph emission show density enhancements of, on average, 7 times background streamer densities are required to fit the bright edges of a number of CME events (Thernisien et al. 2006). Our simulation lacks an inner boundary mass flux (necessary if we were modeling solar wind outflow), so the 10^3 cavity-to-rim variation in density we obtain may be a bit too large; however, during very fast CME events, it is unlikely that mass flow could compensate for the very rapid expansion into the heliosphere.

Figure 9 plots meridional planes of the radial velocity. The shearing motions force a significant expansion velocity until the eruptive flare reconnection. Once the flare reconnection starts, it quickly becomes the dominant component of the velocity signal. The outward portion of the flare reconnection jet fills and accelerates the entire density cavity structure seen in Figure 8. We also capture the strong downflows associated with the inward portion of the flare reconnection jet. Examining the $t = 6750$ and 7500 s frames, we see the flare velocity boost has overtaken the expansion wave and now drives a strong shock, visible as the sharp blue-to-red transition in the color map. The leading edge of the velocity lies right over the dense outer shell corresponding to the bright front seen in the coronagraph observations. In order to further quantify the eruption profile we will examine the height-time plot of the outermost, simply connected field line of the erupting structure.

3.3.2. *Height-Time Profile and Energetics*

Figure 10*a* plots radial distance $h(t)$ of the separatrix surface separating the erupting, highly twisted field structure from the overlying background flux. This distance is measured at 15° latitude in the plane of symmetry $\phi = 0$ and corresponds to the location of the X-line in the 2.5D simulation (Fig. 7 in MacNeice et al. 2004). It is important to note that these distances do not correspond to the location of a material point or plasma parcel, so the velocity of any given field line is likely underestimated using this measure. Before the flare reconnection kicks in, $h(t)$ is gradually increasing due to expansion and the onset of the breakout reconnection above the sheared field flux. There is a clear break associated with the beginning of the flare reconnection and the height-time points after $t = 6750$ are fit well with a constant slope $v_{\rm erupt} = 1135.5$ km s^{-1}. Figure 10*b* plots $v(t) = dh/dt$, the numerical derivative of the height-time points above. Here, we see the velocity increasing linearly during the rising and breakout phase ($a_{\rm rise} = 63.6$ m s^{-2}) followed by an almost steplike increase at the time of the flare reconnection to the average eruption velocity. The rapid acceleration phase lasts for 250 s and corresponding to $a_{\rm flare} = 2966.9$ m s^{-2}. We note the height-time curve and acceleration profile are different than those found by DeVore & Antiochos (2008), and we are continuing our investigation into these differences. A single CME initiation mechanism is likely to produce many different acceleration profiles depending on the properties of the source region and surrounding magnetic environment.

The magnitude and duration of the 3D breakout rapid acceleration phase is quite consistent with observational results. For example, Qiu et al. (2004) measured an erupting filament peak acceleration of 3000 m s^{-2}, St. Cyr et al. (1999) observed a peak acceleration of 3270 m s^{-2}, and Alexander et al. (2002) and Gallagher et al. (2003) found erupting X-ray and EUV features having maximum acceleration on the order of $\gtrsim$1000 m s^{-2}, respectively. Recently, Zhang & Dere (2006) cataloged a broad distribution of magnitudes of the rapid acceleration phase, from 2.8 to 4400 m s^{-2}, and derived a scaling law for the peak acceleration as a function of the duration of acceleration phase. The Zhang & Dere scaling law "predicts" a value of $A = 2398$ m s^{-2} for our simulation acceleration phase duration of 4.17 minutes (250 s)

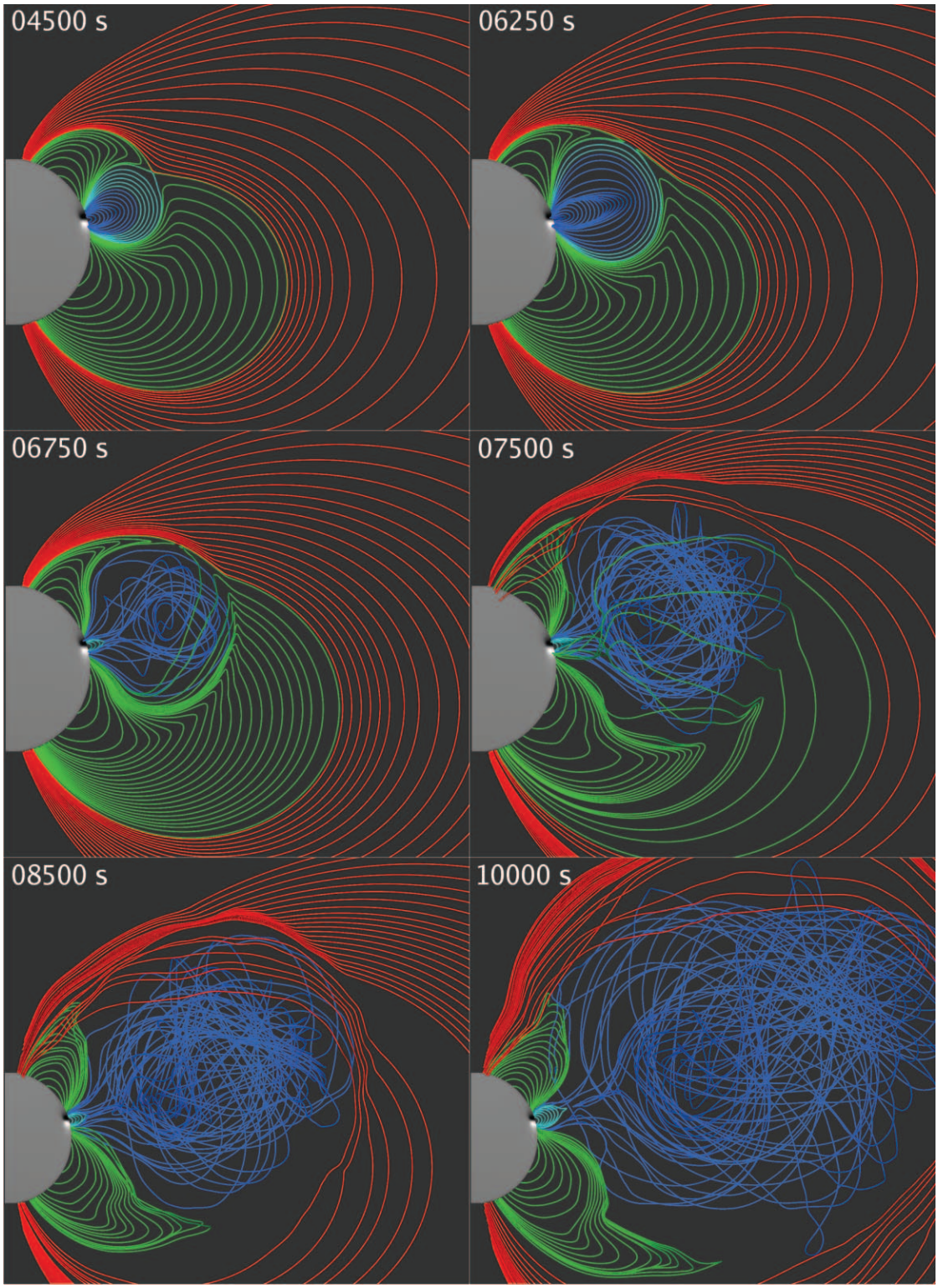

FIG. 7.— Snapshots of the magnetic field evolution during the 3D breakout eruption. Representative field lines are colored in the Antiochos et al. (1999) fashion corresponding to the role the various portions of the flux systems play with respect to the 2.5D scenario. The simulation time is given in the top left corner of each panel and the view is zoomed out in the bottom row to show the complex interaction between the erupting and overlying field as well as the within the erupting field itself by regions of opposite shear.

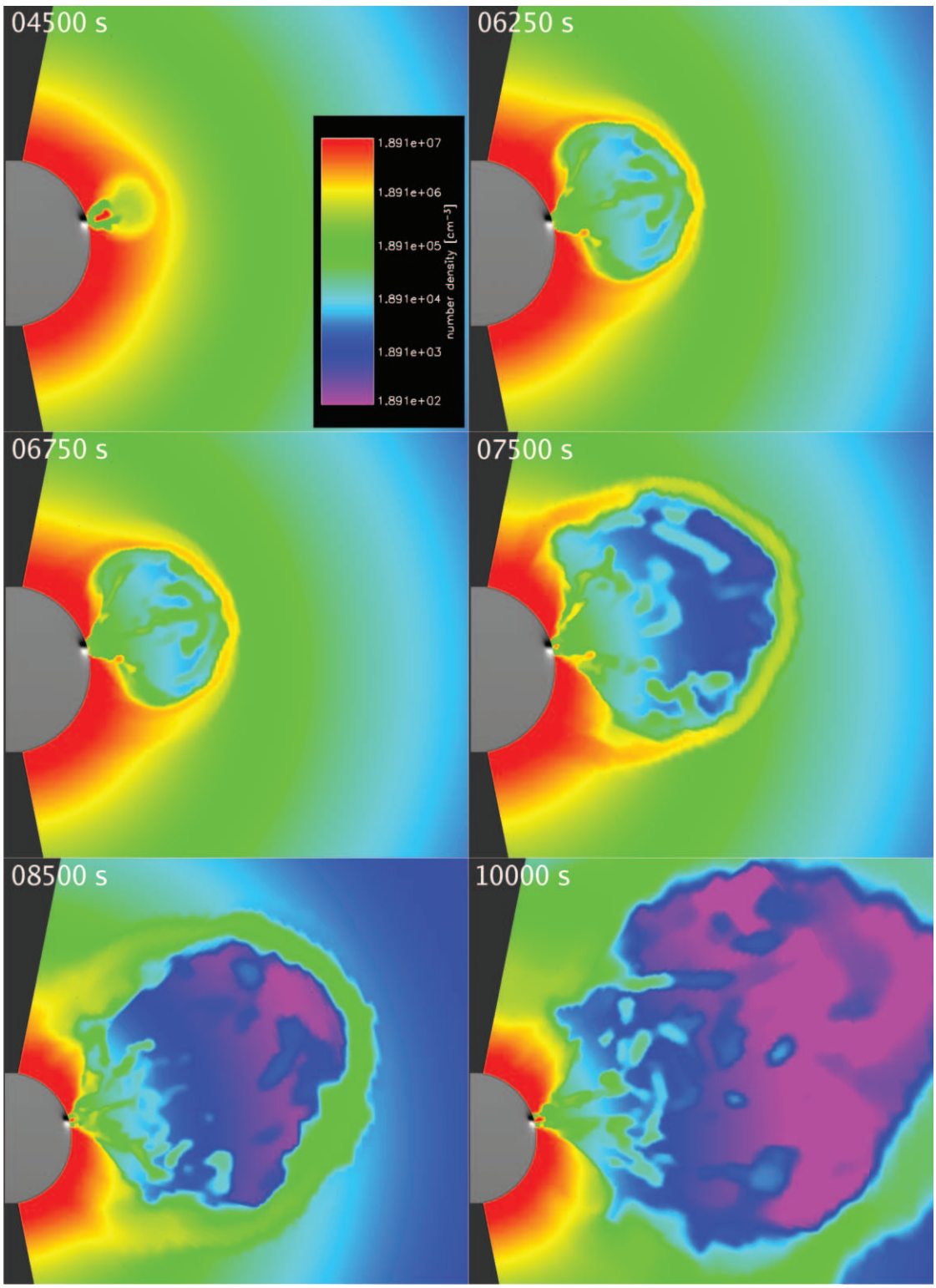

FIG. 8.—Same format as Fig. 7, but showing the $\phi = 0$ meridional cut of mass density. The logarithmic color scale is shown in the first panel.

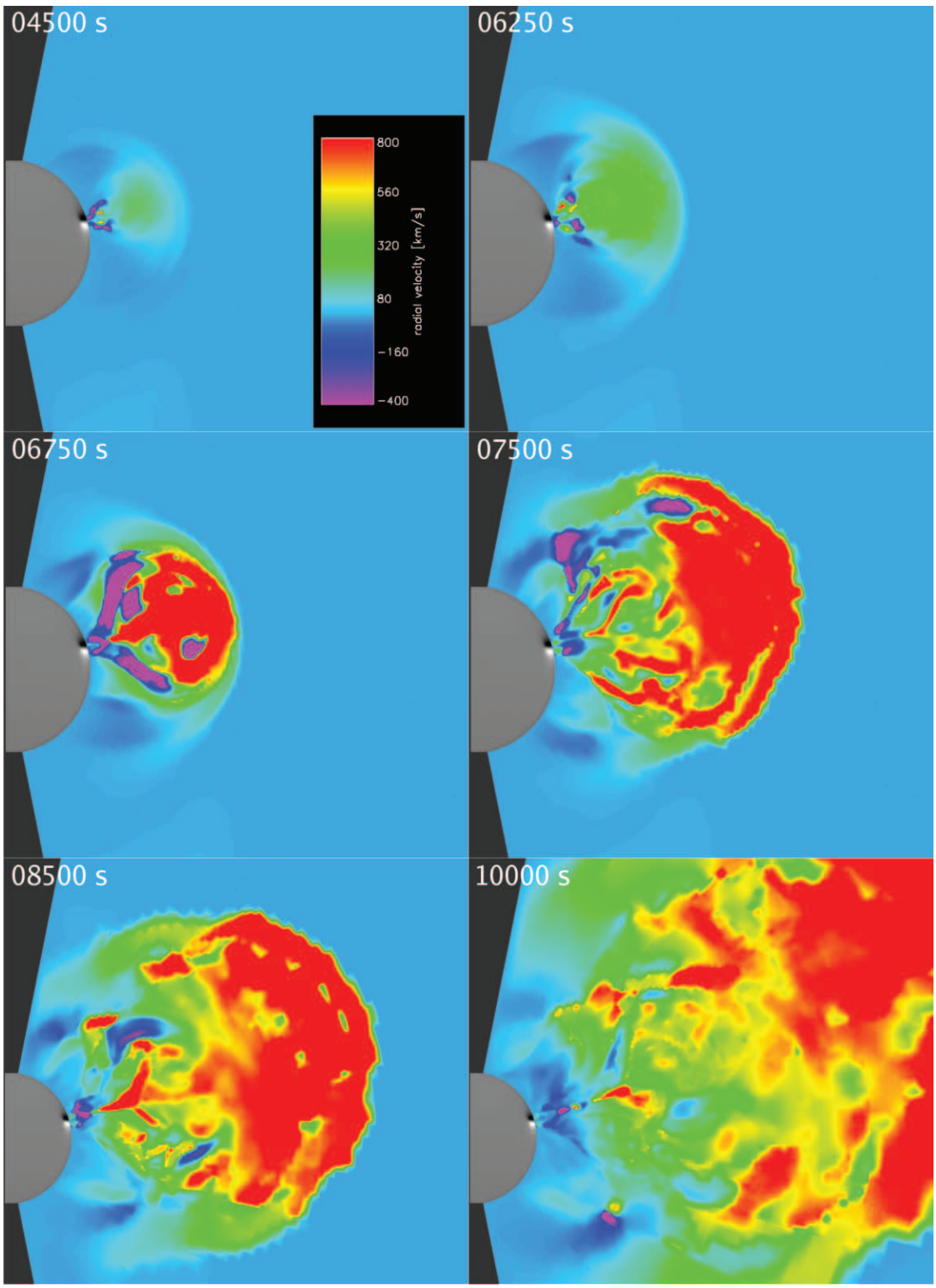

FIG. 9.—Same format as Figs. 7 and 8, but showing the meridional cut of the radial velocity component v_r.

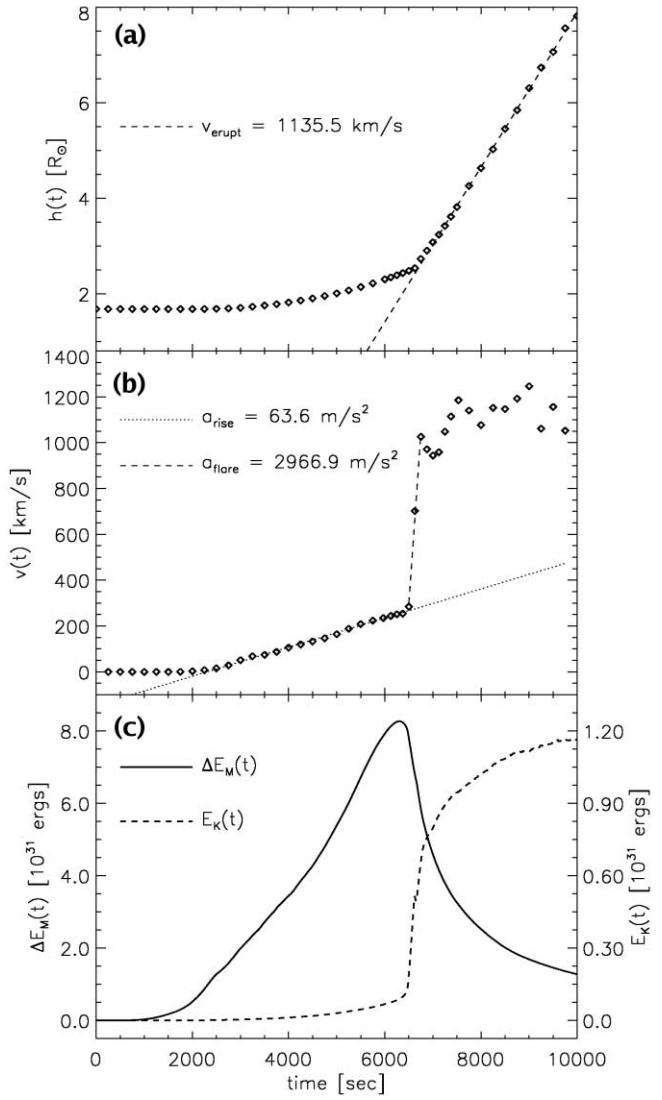

FIG. 10.—(*a*) Plot of the quantity $h(t)$, the radial distance of the separatrix surface at 15° latitude in the plane of symmetry ($\phi = 0$). This is approximately the 3D equivalent of the location of the axisymmetric X-line shown in MacNeice et al. (2004). (*b*) Plot of $v(t) = dh/dt$ showing the clear transition from a linearly increasing rising phase velocity ($a_{\rm rise} \sim 64$ m s^{-2}) through a rapid acceleration phase ($a_{\rm flare} \sim 2970$ m s^{-2}) toward an asymptotic eruption velocity ($v_{\rm erupt} \sim 1100$ km s^{-1}). (*c*) Global magnetic (*solid line*) and kinetic (*dashed line*) energy evolution. The free magnetic energy $\Delta E_M(t)$ is defined as $E_M(t) - E_M(0)$. The rapid release of stored free magnetic energy is seen coinciding with the almost step-function–like increase in kinetic energy. During the 1000 s (16.7 minutes) time interval from $t = 6290$ to 7290 s, approximately 17.8% of the magnetic free energy drop is converted into kinetic energy.

which is in reasonable agreement to our actual $a_{\rm flare}$ value. Schrijver et al. (2008) have argued that during the rapid acceleration phase, erupting filament height observations imply $h \sim t^3$ and are therefore most compatible with the helical kink (Török & Kliem 2005) or torus instabilities (Kliem & Török 2006) when an initial velocity perturbation is introduced. Schrivjer et al. scale their torus instability results to a couple of observed events and obtain acceleration profiles that reach ~1000 m s^{-2} for durations of ~10 minutes. Bong et al. (2006) argue that, in an event with breakout topology, because the main acceleration peak occurs after the visible opening of the overlying field and at about the same time as the maximum flare emission that it cannot be the breakout mechanism responsible for the CME initiation. However, these results show that the acceleration due to the flare reconnection can be quite distinct from the acceleration associated with the breakout reconnection expansion and that in three dimensions the driven flare reconnection can generate a rapid acceleration phase of qualitatively similar magnitude and duration as those observed in the fastest filament eruptions with relative timing that is completely compatible with the Bong et al. (2006) observations.

Figure 10*c* plots the time evolution of the total free magnetic energy $\Delta E_M = E_M(t) - E_M(0)$ and total kinetic energy $E_K(t)$ in the system. The free magnetic energy reaches its maximum value at $t = 6290$ s and from Figures 10*a* and 10*b*, the "impulsive" acceleration due to the upwards flare reconnection jet starts sometime between 6500 and 6750 s. The 1000 s (16.7 minutes) interval starting at the time of the maximum free energy includes the last phases of the preflare runaway breakout reconnection and the initial ("impulsive") phase of the eruptive flare reconnection. The magnitude of the change in free magnetic energy over this period is $|E_M(7290) - E_M(6290)| = 4.567 \times 10^{31}$ ergs, while the associated increase in kinetic energy $E_K(7290) - E_K(6290) = 8.139 \times 10^{30}$ ergs. Thus, 17.8% of the available free magnetic energy is converted directly into kinetic energy during the interval including the "impulsive" phase of the eruption. However, in the subsequent "gradual" phase of the flare reconnection, the free magnetic energy continues to drop and by the end of the simulation, the total change in free magnetic energy has reached 7.0×10^{31} ergs with a corresponding total kinetic energy of 1.164×10^{31} ergs, or 15.4% of the dissipated free magnetic energy.

3.3.3. *Breakout and Flare Reconnection*

The left panel of Figure 11 plots several representative field lines illustrating the breakout reconnection process at time $t = 6250$ s. The green field lines correspond to newly created "side-arcade" flux formed by reconnection between the light blue unsheared field above the expanding sheared component and the red restraining background flux. The right panel plots an isosurface of the ϕ-component of current density at $j_\phi = +0.30$ statamp cm^{-2}. The current structure(s) on the solar surface and at the base of the expanding field region are due to the imposed boundary motions, but the dome like sheet that forms on the separatrix boundary surrounding the expanding sheared field is a topologically induced response. MacNeice et al. (2004) showed that with sufficient resolution, the axisymmetric simulation breakout results were independent of the grid size. For 3D calculations, we still do not have the computational capacity to perform a similar study, but we expect the same results. Given that the mechanism for "triggering" the breakout reconnection is numerical resistivity, future work must include characterizing the effects of enhanced resolution on the rate or character of magnetic reconnection. It may be possible to mitigate some of the increased computational costs through solution-adaptive grid refinement in regions of current sheet formation.

A snapshot of the eruptive flare reconnection at $t = 6750$ s is shown in Figure 12. Both panels show the same set of representative flare loops (*yellow region*) and newly reconnected field lines that are becoming highly twisted and part of the erupting flux (*white region*). The left panel plots the $\phi = 0$ meridional plane of radial velocity showing the structure of the outflow jets associated with the eruptive flare reconnection. Maximum upwards velocities exceeding $v_r \gtrsim 4000$ km s^{-1} (comparable to Alfvén speed at this radius) are observed in a narrow sheet above the recently formed flare arcade, as well as significant downflows along the flare-loop legs ($v_r \lesssim -2000$ km s^{-1}). The intensity of these flows diminish with time but the flare reconnection and the jet structure continues for the duration of the simulation (see Figs. 7*e* and 7*f*). The right panel shows the 3D equivalent of the well known

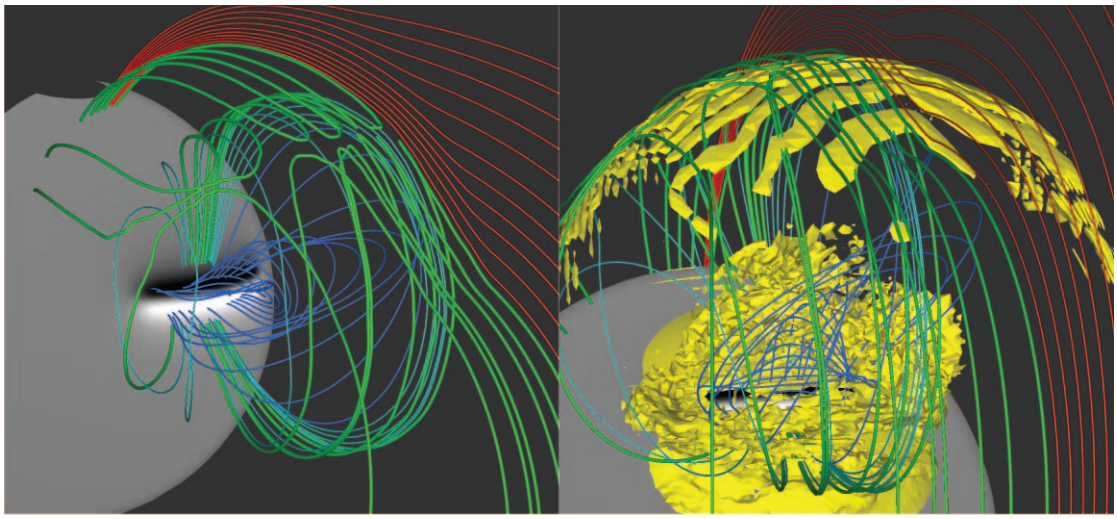

FIG. 11.—*Left*: Several representative field lines at $t = 6250$ s during the breakout reconnection phase (in Figs. 1*b* and 2*b*). The newly reconnected side-arcade field lines are shown in green, the unsheared inner-arcade field lines are shown in light blue, the highly stressed, expanding inner-arcade field is dark blue, and the overlying flux is shown in red. *Right*: Same field lines (from a different perspective) as well as an isocontour of $j_\phi = 0.30$ statamp cm^{-2}, depicting the current sheet formed along the separatrix boundary of the stressed inner-arcade flux system. See text for details.

2D CHSKP eruptive flare current sheet as an isosurface of $j_\phi = -4.5$ statamp cm^{-2} in orange. While we capture the large scale properties, there is so much physical structure at (and below) our numerical resolution limit, many important features are still not resolved. For example, flare reconnection is known to be patchy (e.g., Linton & Longcope 2006; Linton et al. 2007) and high cadence, high-resolution solar observations have shown a wealth of fine structure and dynamics, such as coronal downflows (Sheeley et al. 2004), flare ribbon and loop evolution, and bursty emission in a variety of wavelengths. Also, details of the reconnection jet structures, such as the shocks and turbulence formed from the Alfvénic outflows have direct implications for flare heating, accelerating solar energetic particles, and a host of other related features (see Benz 2008, and references therein).

4. DISCUSSION

In the first half of the paper, we discussed the topological evolution of the magnetic breakout eruption process and showed that a 3D system with two polarity inversion lines, a separatrix dome, a pair of spline lines and a single 3D null point meets the minimum required complexity for the breakout process to operate. In the second half, we presented MHD simulation results of a fast breakout CME that reaches an asymptotic eruption velocity of $\sim$1100 km s^{-1} within 3 $R_\odot$. The eruptive flare onset and impulsive phase generate a prompt rapid acceleration phase of $a_{\rm flare} \sim$ 2970m s^{-2} for 4.2 minutes, in reasonable agreement with observations. The bulk of this acceleration is associated with the impressive flare reconnection jets, with maximum radial velocities of $v_r \sim 4000$ km s^{-1} upwards and $\sim$2000 km s^{-1} downwards. Overall, the CME eruption releases 7.0×10^{31} ergs of free magnetic energy with 15.4% of that converted into a total kinetic energy of 1.16×10^{31} ergs by the end of the simulation. We expect that this fraction will increase with higher numerical resolution, i.e., lower effective resistivity. Remarkably complex ejecta fields arise from internal reconnection between the oppositely directed shear layers and continued interaction between the erupting and overlying

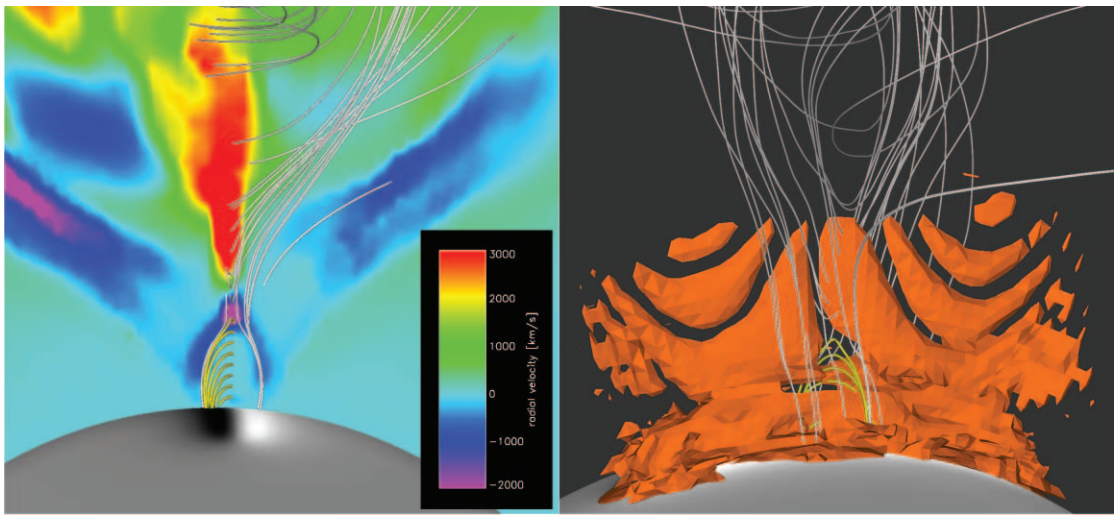

FIG. 12.—*Left*: Eruptive flare loop geometry at $t = 6750$ s in the flare reconnection phase (Fig. 1*c* and 2*c*) along with a semitransparent meridional plane of v_r to show the structure of the reconnection jets. At this time step, the upward jet maximum velocities exceed 4000 km s^{-1}, while the downward jet contains -2000 km s^{-1} maximum flow speeds. *Right*: Same field lines from a different perspective, showing a top-down polar view of the azimuthal extent of the radial current sheet. The orange isosurface is of $j_\phi = -4.50$ statamp cm^{-2}. See text for details.

fields. Since only 30%–50% of in situ ICME fields show coherent flux-rope structures (Gosling 1990; Cane et al. 1997), these results may be an indication of some of the processes responsible for producing complex events. Another important feature of the simulation results is the lack of large-scale, persistent magnetic islands forming in front of the erupting flux rope structure that were seen in previous axisymmetric configurations with equatorial symmetry (e.g., MacNeice et al. 2004; van der Holst et al. 2007). These islands have the effect of slowing the eruption down; thus, despite our latitudinally extended, quasi two-dimensional magnetic configuration, having a fully three dimensional simulation allows us to avoid this undesirable feature.

While these simulation results show that the magnetic breakout model in three dimensions can account for the majority of the large scale properties of fast CMEs, there are still a number of weaknesses that will need to be addressed in future work. First, the magnetic shear distribution, while mathematically convenient in the calculation of free magnetic energy, is generally more complex than the shear observed with vector magnetograms or inferred from scalar magnetogram feature tracking. Second, our sunspot structure is too artificial. The magnetic configuration does approximate the "narrowness" of erupting filaments and their associated shear channels, but the shape is too extended and the field strength ratio of our active region to background is too low (25 : 1 compared to typical solar values of hundreds : 1). Third, our spherically symmetric solar atmosphere needs to be replaced with a nonuniform distribution so that, together with the field distribution, the whole system has a more uniform, low plasma β. Finally, there is too much structure at the grid scale. Attempting to model a realistic solar case without sufficient resolution runs the risk of losing the most important science. Current limitations aside, the results presented herein are encouraging; with the magnetic complexity of the simplest, nontrivial 3D field configuration composed of basically two dipoles, the magnetic breakout process can produce a fast CME without requiring a preeruption flux rope of any sort.

B. J. L. gratefully acknowledges current support from the NSF SHINE program ATM-0621725 and additional funding from NASA, the Office of Naval Research (ONR), and SSL/UCB participation in the Center for Integrated Space-weather Modeling (CISM) collaboration. The DoD High Performance Computing Modernization Program provided resources at the ERDC major shared resource and NRL-DC distributed computing centers for this research. This work was supported, in part, by the NASA HTP, TR&T, and SR&T programs.

REFERENCES

Alexander, D., Metcalf, T. R., & Nitta, N. V. 2002, Geophys. Res. Lett., 29, 41
Antiochos, S. K. 1998, ApJ, 502, L181
Antiochos, S. K., DeVore, C. R., Karpen, J. T., & Mikic, Z. 2007, ApJ, 671, 936
Antiochos, S. K., DeVore, C. R., & Klimchuk, J. A. 1999, ApJ, 510, 485
Attril, G. D. R., Harra, L. K., van Driel-Gesztelyi, L., & Dèmoulin, P. 2007, ApJ, 656, L101
Attril, G. D. R., Nakwacki, M. S., Harra, L. K., van Driel-Gesztelyi, L., Mandrini, C. H., Dasso, S., & Wang, J. 2006, Sol. Phys., 238, 117
Aulanier, G., DeLuca, E. E., Antiochos, S. K., McMullen, R. A., & Golub, L. 2000, ApJ, 540, 1126
Benz, A. O. 2008, Living Rev. Sol. Phys., 5, 1, http://www.livingreviews.org/lrsp-2008-1
Bong, S.-C., Moon, Y.-J., Cho, K.-S., Kim, Y.-H., Park, Y. D., & Choe, G. S. 2006, ApJ, 636, L169
Cane, H. V., Richardson, I. G., & Wibberenz, G. 1997, J. Geophys. Res., 102, 7075
Carmichael, H. 1964, in The Physics of Solar Flares, ed. W. N. Hess (NASA SP-50; Washington: NASA), 451
Crooker, N. U., Gosling, J. T. & Kahler, S. W. 2002, J. Geophys. Res., 107, A2, 1018
Deng, N., Liu, C., Yang, G., Wang, H., & Denker, C. 2005, ApJ, 623, 1195
DeVore, C. R. 1991, J. Comput. Phys., 92, 142
DeVore, C. R., & Antiochos, S. K. 2005, ApJ, 628, 1031
———. 2006, BAAS, 38, 236
———. 2008, ApJ, 680, 740
Forbes, T. G., & Lin, J. 2000, J. Atmos. Sol.-Terr. Phys., 62, 1499
Forbes, T. G., et al. 2006, Space Sci. Rev., 123, 251
Gallagher, P. T., Lawrence, G. R., & Dennis, B. R. 2003, ApJ, 588, L53
Gao, J., MacNeice, P. J., & Antiochos, S. K. 2004, AGU, Fall Meeting (Abstr. SH13A-1151; Washington: AGU)
Gary, G. A., & Moore, R. L. 2004, ApJ, 611, 545
Gosling, J. T. 1990, in Physics of Magnetic Flux Ropes, ed. C. T. Russell, E. R. Priest, & L. C. Lee (Washington: AGU), 9
Gosling, J. T., Birn, J., & Hesse, M. 1995, Geophys. Res. Lett, 22, 869
Hirayama, T. 1974, Sol. Phys., 34, 323
Joshi, B., Manoharan, P. K., Veronig, A. M., Pant, P., & Pandey, K. 2007, Sol. Phys., 242, 143
Kliem, B., & Török, T. 2006, Phys. Rev. Lett., 96, 255002
Kopp, R. A., & Pneuman, G. W. 1976, Sol. Phys., 50, 85
Li, Y., & Luhmann, J. G. 2006, ApJ, 648, 732
Li, Y., Lynch, B. J., Stenborg, G., Luhmann, J. G., Huttunen, K. E. J., Welsch, B. T., Liewer, P. C., & Vourlidas, A. 2008, ApJ, 681, L37
Linker, J. A., Mikić, Z., Lionello, R., Riley, P., Amari, T., & Odstrcil, D. 2003, Physics of Plasmas, 10, 1971
Linton, M. G., DeVore, C. R., & Longcope, D. W. 2007, preprint (arXiv: 0712.1235)
Linton, M. G., & Longcope, D. W. 2006, ApJ, 642, 1177
Liu, C., Lee, J., Deng, N., Gary, D. E., & Wang, H. 2006, ApJ, 642, 1205
Lynch, B. J., Antiochos, S. K., MacNeice, P. J., Zurbuchen, T. H., & Fisk, L. A. 2004, ApJ, 617, 589
MacNeice, P. J., Antiochos, S. K., Phillips, A., Spicer, D. S., DeVore, C. R., & Olson, K. M. 2004, ApJ, 614, 1028
MacNeice, P. J., Olson, K. M., Mobarry, C., de Fainchtein, R., & Packer, C. 2000, Comput. Phys. Commun., 126, 330
Manoharan, P. K., & Kundu, M. R. 2003, ApJ, 592, 597
Moore, R. L., Sterling, A. C., Hudson, H., & Lemen, J. R. 2001, ApJ, 552, 833
Owens, M. J. & Crooker, N. U. 2006, J. Geophys. Res., 111, A10, A10104
Peng, Z., & Hu, Y.-Q. 2007, ApJ, 668, 513
Phillips, A., MacNeice, P. J., & Antiochos, S. K. 2005, ApJ, 624, L129
Pohjolainen, S., Vilmer, N., Khan, J. I., & Hillaris, A. E. 2005, A&A, 434, 329
Qiu, J., Wang, H., Cheng, C. Z., & Gary, D. E. 2004, ApJ, 604, 900
Roussev, I. I., Lugaz, N., & Sokolov, I. V. 2007, ApJ, 668, L87
Roussev, I. I., Sokolov, I. V., Forbes, T. G., Gombosi, T. I., Lee, M. A., & Sakai, J. I. 2004, ApJ, 605, L73
Schrijver, C. J., Elmore, C., Kliem, B., Török, T., & Title, A. M. 2008, ApJ, 674, 586
Sheeley, N. R., Jr., Warren, H. P., & Wang, Y.-M. 2004, ApJ, 616, 1224
St. Cyr, O. C., Burkepile, J. T., Hundhausen, A. J., & Lecinski, A. R. 1999, J. Geophys. Res., 104, 12493
Sterling, A. C., & Moore, R. L. 2001, ApJ, 560, 1045
———. 2004, ApJ, 602, 1024
Sturrock, P. A. 1968, in IAU Symp. 35, Structure and Development of Solar Active Regions, ed. K. O. Kiepenheuer (Dordrecht: Reidel), 471
Thernisien, A. F. R., Howard, R. A., & Vourlidas, A. 2006, ApJ, 652, 763
Török, T., & Kliem, B. 2005, ApJ, 630, L97
Ugarte-Urra, I., Warren, H. P., & Winebarger, A. R. 2007, ApJ, 662, 1293
van der Holst, B., Jacobs, C., & Poedts, S. 2007, ApJ, 671, L77
Wang, T., Yan, Y., Wang, J., Kurokawa, H., & Shibata, K. 2002, ApJ, 572, 580
Yurchyshyn, V., Karlický, M., Hu, Q., & Wang, H. 2006, Sol. Phys., 235, 147
Zhang, J., & Dere, K. P. 2006, ApJ, 649, 1100
Zhang, Y. Z., Wang, J. X., & Hu, Y. Q. 2006, ApJ, 641, 572